Progress In Electromagnetics Research C, Vol. 108, 63–78, 2021

High Gain Dielectric Resonance Antenna Array for Millimeter Wave Vehicular Wireless Communication

Wei Luo[1, *], Linsong Shi[1], Wenwen Xu[1], Wuquan Chen[1], Yuqi Yang[2], and Yi Ren[1]

Abstract—This paper presents a high gain dielectric resonance antenna (DRA) array for vehicular wireless communication and 5G system in millimeter wave band, which takes the advantage of low side lobe level (SLL). The planar antenna array is composed of 8×8 rectangular DRA elements, whose operation mode is the fundamental mode TE_{111}. The beamforming weights of the array are designed based on the principle of Dolph-Chebyshev distribution to suppress the antenna SLL. The planar array consists of 8 linear sub-arrays, which are fed with standing-wave series resonance method respectively. The excitations of sub-array elements are precisely adjusted based on the aperture coupling model. Furthermore, the series-parallel hybrid feed network and parallel-cascaded feed network are applied to unequally feed the sub-arrays in accordance with Chebyshev polynomials. The measurement results of prototype validate the design solution of antenna array. The impedance bandwidth is 570 MHz (25.77 GHz–26.34 GHz) for reflection coefficients less than -10 dB, and the antenna gain and SLL are 20.5 ± 1 dBi and 20 dB, respectively. Due to the advantages of miniaturization and narrow beam, the proposed DRA antenna array is adequate for vehicle communication equipment.

1. INTRODUCTION

The Internet of Vehicle (IoV) has become a significant application scenario of the fifth-generation mobile communication system (5G), in which vehicle antenna is the critical equipment for transmitting information in air interface [1]. Although traditional automotive antennas, such as broadcast antennas and satellite navigation antennas, have been widely deployed in various automotive products, 5G millimeter wave communication system has put forward crucial requirements for the performance of vehicle antennas and vehicle RF front-end [2, 3]. Limited by the overall vehicle design, the performance improvement and compactness design of vehicle antenna are currently important research issues for vehicular wireless communication [4–6].

According to the particularity of vehicle mobile carrier platform, traditional vehicle antenna research focuses on the integrated design of FM broadcast antenna and LTE antenna. One of the most popular combinations of multi-frequency and multi-standard antenna is shark-fin antenna, which integrates multiple input–multiple-output (MIMO)-LTE, FM, and GPS antenna into one radome meeting the requirements of automotive aerodynamics. Meanwhile, the planar antenna array with high gain is widely researched for millimeter wave vehicle radar and Dual-Function Radar Communication (DFRC) system [7]. For miniaturization purpose of electronic devices, the corporate stacked microstrip and substrate integrated waveguide (SIW) feeding structure are used for the patch antenna array, whose radiators consist of slim rectangular patches with surrounding U-shaped parasitic elements [8]. On the other hand, vehicle antennas can also be deployed on windows. The traditional windscreen antennas have been extensively applied by automobile manufacturers, which are commonly the meandering line

Received 1 November 2020, Accepted 15 December 2020, Scheduled 3 January 2021
* Corresponding author: Wei Luo (luowei1@cqupt.edu.cn).
[1] College of Electronic Engineering, Chongqing University of Posts and Telecommunications, Chongqing, China. [2] Electronic Information and Networking Research Institute, Chongqing University of Posts and Telecommunications, Chongqing, China.

made of metal wire and processed inside the windshield. Due to the difficulty in impedance matching and poor radiation performance, windscreen antennas are only implemented as receivers for broadcast communication. With the development of material science, a novel transparent glass antenna is proposed for the 28 GHz band wireless communication between the base station and vehicles, which is virtually a patch antenna fabricated with synthetic fused silica glass. The glass antennas could be attached to the window surface and do not obstruct the view of drivers [9, 10]. Moreover, the dual-band optically transparent antenna based on a slotted interconnected ring resonator is structured on a plexiglass substrate with Silver Tin Oxide as transparent conducting material, which could be utilized for the 2×2 MIMO transceiver system [11].

Dielectric resonator antenna (DRA) has the advantages of high degree of freedom, rich resonant modes, small size, wide frequency band and high radiation efficiency, which is promising for the vehicle wireless communication equipment [12]. The sectorization technique in the hemispherical DRA is investigated for optimization of antenna parameters with the sector angle [13]. The aperture coupling method is applied for cylindrical dielectric resonator antenna, which could excite six different hybrid radiating modes [14]. In order to excite two radiation modes simultaneously, the DRA is separated into an inner cylindrical dielectric resonator and an outer ring one, which are both embedded in a SIW cavity. Meanwhile, the impedance bandwidth and directivity of the DRA is greatly improved by the two nearly degenerate modes and surrounding SIW cavity [15]. Since the vehicular mobile station needs to communicate with the base station with high gain beam, it is necessary to design reasonable feed network for the DRA array. In view of the convenience of integration, regular rectangular DRA array could be fed by the SIW feeding network. Furthermore, single DRA radiator could be fed by SIW slots to obtain multiple operation modes [16].

This paper proposes a planar array of DRAs for the vehicle communication, which possesses the advantage of low side lobe level (SLL). Section 2 presents the design principle of rectangular DRA. In Section 3, the feeding methods are investigated for the side lobe suppression, with which the planar antenna arrays are designed and analyzed. The prototype and measurements are presented to validate the proposed design method in Section 4.

2. DESIGN OF RECTANGULAR DIELECTRIC RESONATOR ANTENNA

Compared with other DRAs, such as semi-spherical and cylindrical DRA, the rectangular DRA shown in Fig. 1(a) has the advantages of stable radiation mode and easy fabrication [17, 18]. The equivalent RLC circuit is shown in Fig. 1(b). Considering the six surfaces of the rectangular DRA as perfect magnetic surface (PMC), the relationship between wave number and DRA size is given based on Segregation Variable Method

$$\begin{cases} k_x = \dfrac{\pi}{a} \\ k_y = \dfrac{\pi}{b} \\ k_z \tan\left(\dfrac{k_z d}{2}\right) = \sqrt{(\varepsilon_r - 1)k_0^2 - k_z^2} \\ k_x^2 + k_y^2 + k_z^2 = \varepsilon_r k_0^2 \end{cases} \tag{1}$$

where k_0 is the wave number in the vacuum. k_x, k_y, and k_z are the components of wave number along the x, y, and z axis directions inside the DRA region. ε_r is the relative permittivity of the DRA. The resonant operating frequency is given based on the analysis of resonance mode

$$f_r\,(m,n,p) = \frac{c}{2\pi\sqrt{\varepsilon\mu}}\sqrt{\left(\frac{m\pi}{a}\right)^2 + \left(\frac{n\pi}{b}\right)^2 + \left(\frac{p\pi}{d}\right)^2} \tag{2}$$

Since the antenna patterns should keep directional and stable, the dominant mode TE_{111} is selected as the operation mode. According to the requirements of vehicle communication protocol standard and 5G New Radio (NR) [19], 26 GHz is the central operation frequency of the DRA element. Thus, the size of the DRA could be estimated with Equation (2), and the antenna operation parameters are shown in Table 1 in detail. Considering the feasibility of fabrication and antenna performance, a rectangular dielectric cube with a relative dielectric constant of $\varepsilon_r = 10.2$ is selected as the DRA processing material.

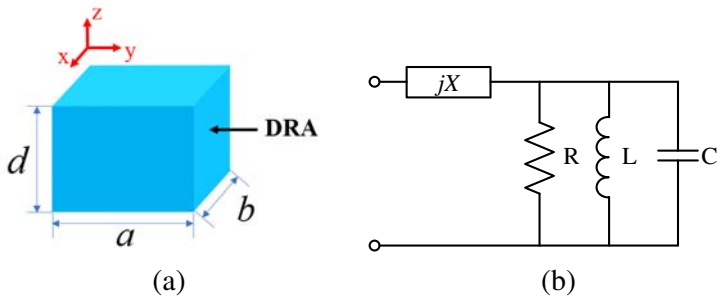

Figure 1. Principle diagram of rectangular DRA. (a) Rectangular DRA with a, b, and d dimensions. (b) Rectangular DRA equivalent RLC circuit.

Table 1. Design index of 26 GHz DRA element.

Parameter	Polarization	Frequency	VSWR	Return Loss
Index	Vertical Polarization	26 GHz	< 2	< -10

The DRA is generally fed with the probe or coupling aperture. The coupling aperture has less influence on the internal resonance mode of dielectric resonator, which could also effectively extend the impedance matching bandwidth. Thus, the DRA is fed with rectangular slots in this paper. The geometry structure of DRA element is shown in Fig. 2. The dielectric cube is placed on the ground of the PCB. The electromagnetic energy is fed into the rectangular slots of the floor through microstrip line on the other side of PCB board, and then coupled into the cube radiator by the rectangular slot. The advantages of this structure are simplicity and stabilization. The detailed engineering parameters of DRA element are shown in Table 2, in which the DRA and substrate are Rogers RT/duroid 6010 and Arlon DiClad 880, respectively.

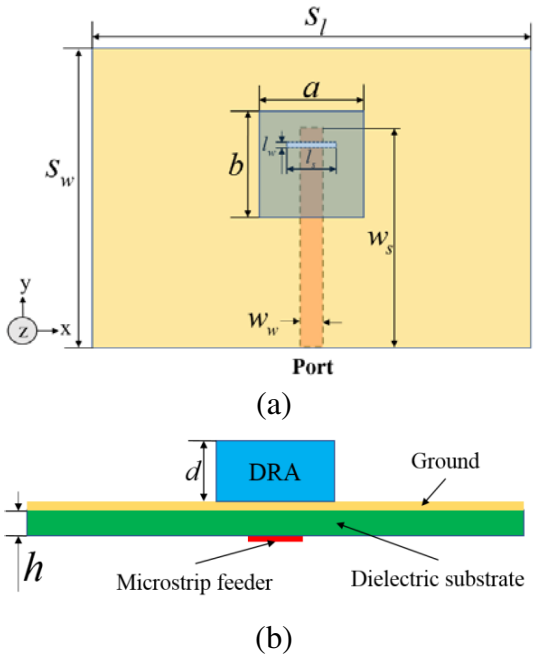

Figure 2. Configuration of rectangular DRA element. (a) Top view. (b) Side view.

Table 2. DRA element structure parameters (unit: mm).

Parameter	a	b	d		Rogers RT/duroid 6010
Value (mm)	4.5	4.5	1.27		
Parameter	l_s	l_w	w_s	w_w	Perfect Electric Conductor
Value (mm)	2.28	0.1	8.5	0.74	
Parameter	h	s_w	s_l		Arlon DiClad 880
Value (mm)	0.254	11.5	16		

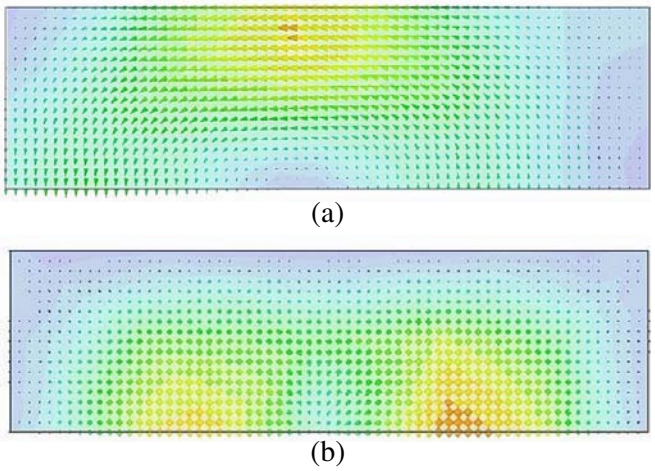

Figure 3. Simulated field distribution inside the DRA. (a) Electric field **E**. (b) Magnetic field **H**.

When the size of DRA and operation frequency are determined, the input impedance matching and resonance mode of the antenna are directly related to the position and size of the feeding slot. The eigenmode method is used to simulate and analyze the magnetic field distribution in different operation modes of rectangular dielectric resonator. Then, the feeding slot is located at the center of the bottom surface of DRA, where the magnetic field is the strongest. Furthermore, the sizes of DRA and feeding slot are optimized with electromagnetic simulation.

The simulated electric field **E** and magnetic field **H** inside the DRA fed with slots are shown in Fig. 3. The operation frequency is 26 GHz, and the TE_{111} mode is excited in the dielectric cube. It is apparent that the distributions of **E** and **H** are generally regular in the radiator of DRA. Moreover, there is little disturbance of **H**, which indicates the components of higher order modes. Nevertheless, the antenna performance primarily depends on the fundamental mode TE_{111}. The simulation of antenna performance is shown in Fig. 4. The impedance bandwidth is 24.69 GHz $\sim$ 26.72 GHz, which meets the requirements of 5G vehicle communication frequency band [19]. Moreover, the antenna element pattern presents the characteristics of directional radiation. While the antenna gain is 6.0 dBi, the half-power beam width (HPBW) is 74°. It is found that the radiation feature is suitable for the highly directional planar arrays.

3. DESIGN OF HIGH GAIN PLANAR ARRAY

For the vehicle DFRC communication in 5G system, high-speed data transmission is achieved by high gain beam, when the vehicle mobile stations communicate with each other. Therefore, it is necessary to utilize planar antenna array combined with complex feed network to realize beamforming and sidelobe suppression [20, 21]. The 8×8 planar array is designed with rectangular DRA elements, which consists

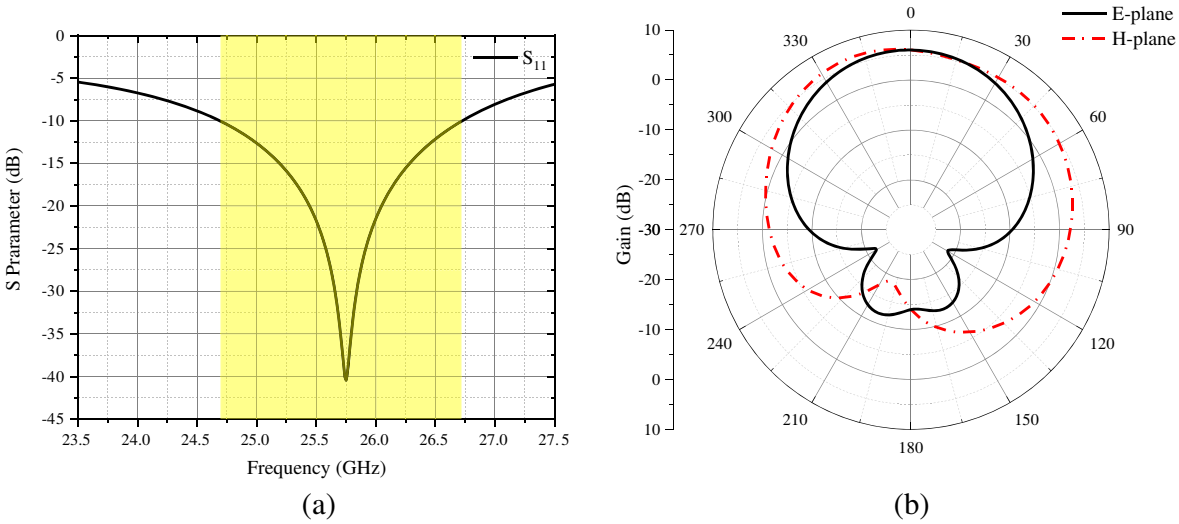

Figure 4. Simulated antenna performance of DRA element. (a) S parameters. (b) Radiation patterns.

of eight 8-element linear arrays in parallel. The normal radiation high gain pattern is beam-formed by adjusting the coupling feed in each linear array. Then, the 3-D high directional beam is designed by the unequal power division feed network connected to linear arrays.

3.1. Low Side Lobe Level Linear Array

The 8-element linear array is fed by standing wave series resonance method, which takes the advantage of simple structure and low feeder loss, as shown in Fig. 5. The excitation weights of elements are tuned with the width of DRA, the length of feeding slot, and the relative position of the slot, which lead to effective suppression of side lobe level [22].

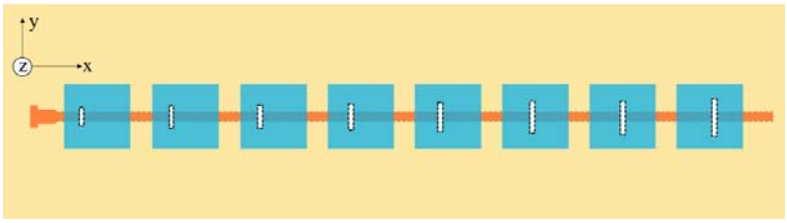

Figure 5. Configuration of 8-element line array.

Due to the narrow band effect of series feed circuit, the structural parameters are optimized to extend the impedance bandwidth. Furthermore, the magnitudes of excited electric field for each array element are designed to approach the Dolph-Chebyshev distribution. Since the adjacent elements should be fed in the same phase, the interval of array elements is usually designed to be about one wavelength.

The equivalent circuit model of slots coupled DRA is shown in Fig. 6, in which the characteristic impedance of DRA is equivalently presented with R_r, C_r, and L_r. Equivalent capacitance C_{Slot} is related with the size of slot, and the microstrip transmission line is generally used as the feed line. The coupling feed relationship between the slot and dielectric radiator is modeled by the transformer model with change ratio of $1 : n$. The magnitude of fed current could be controlled with n value, which is closely related with the size of feeding slot. Therefore, the reasonable proportion relationship of n can be designed for each array element based on Chebyshev polynomial to reduce the SLL for the linear antenna array [23].

The size and relative position of the slots corresponding to each element are tuned to optimize the

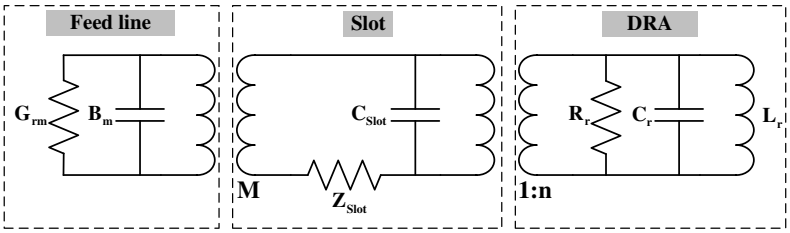

Figure 6. Equivalent circuit model diagram of DRA fed by aperture.

fed electric current. The magnetic field coupling is enhanced with the increase of slot length. On the other hand, if the slot position deviates from the center of the array element along the feed direction, the coupling ability apparently degrades. The input impedance of slot to radiator is influenced by the length and position of slot. Due to the design complexity caused by multifactor variable of fed current, the linear array optimization is decomposed into several steps. Based on the theoretical prediction, the feeding slots are fixed at the center of each DRA element, and all the lengths of rectangular slots are $l_s = 1.98\,\text{mm}$. The length a of the array element is slightly reduced from the middle to the two sides. Fig. 7 shows the distribution of electric field **E** inside the antenna array. It is found that the field intensity distribution gradually decreases along the direction of electromagnetic energy transmission.

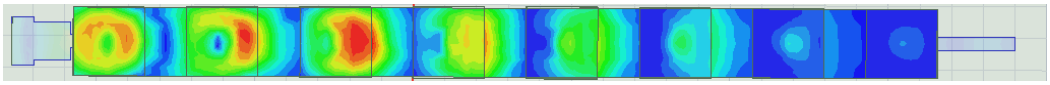

Figure 7. Electric field distribution of linear array with fixed slot position.

Then, the lengths of slots are optimized, while the slot positions keep unchanged. The optimized lengths of the slots are

$$l_s = 0.3i + 0.88\,\text{mm} \quad (i = 1, 2, 3, \ldots, 8) \tag{3}$$

where i is the serial number of array elements, which are numbered sequentially from the feed port to the array end. The width of slot keeps 1 mm. Furthermore, based on the local optimization model, the position and length of the slots are optimized simultaneously. The distribution of electric field **E** shows the characteristics of decreasing from the array middle to both sides, as shown in Fig. 8, which is similar to that of Chebyshev synthesis.

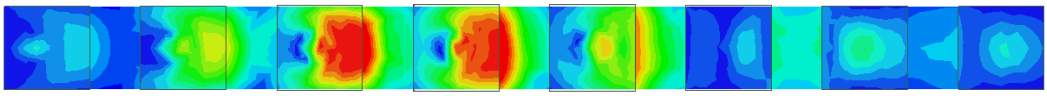

Figure 8. Electric field distribution of linear array with optimized slot position and length.

Based on the optimal design of coupling feed parameters, the S parameter and radiation pattern of 8-element linear array are simulated, as shown in Fig. 9. By adjusting the open stub at the end of microstrip line, good impedance matching can be achieved in the expected frequency band (25.45 GHz–26.30 GHz). Due to the beam forming design based on Chebyshev polynomials in the E-plane, the radiation pattern with low SLL characteristics ($-23.44\,\text{dB}$) is realized. In addition, the beamwidth of the pattern is 60° in the H-plane, since there is only one single element in yoz-plane. The gain of this linear array reaches 14.42 dBi, and the main lobe width is 13.45°.

3.2. Unequal Power Divided Feed Network and Planar Array

The 8-element linear array is combined into an 8×8 planar array. Two different feed structures, series-parallel hybrid feed network and parallel-cascaded feed network, are attempted to feed the planar array.

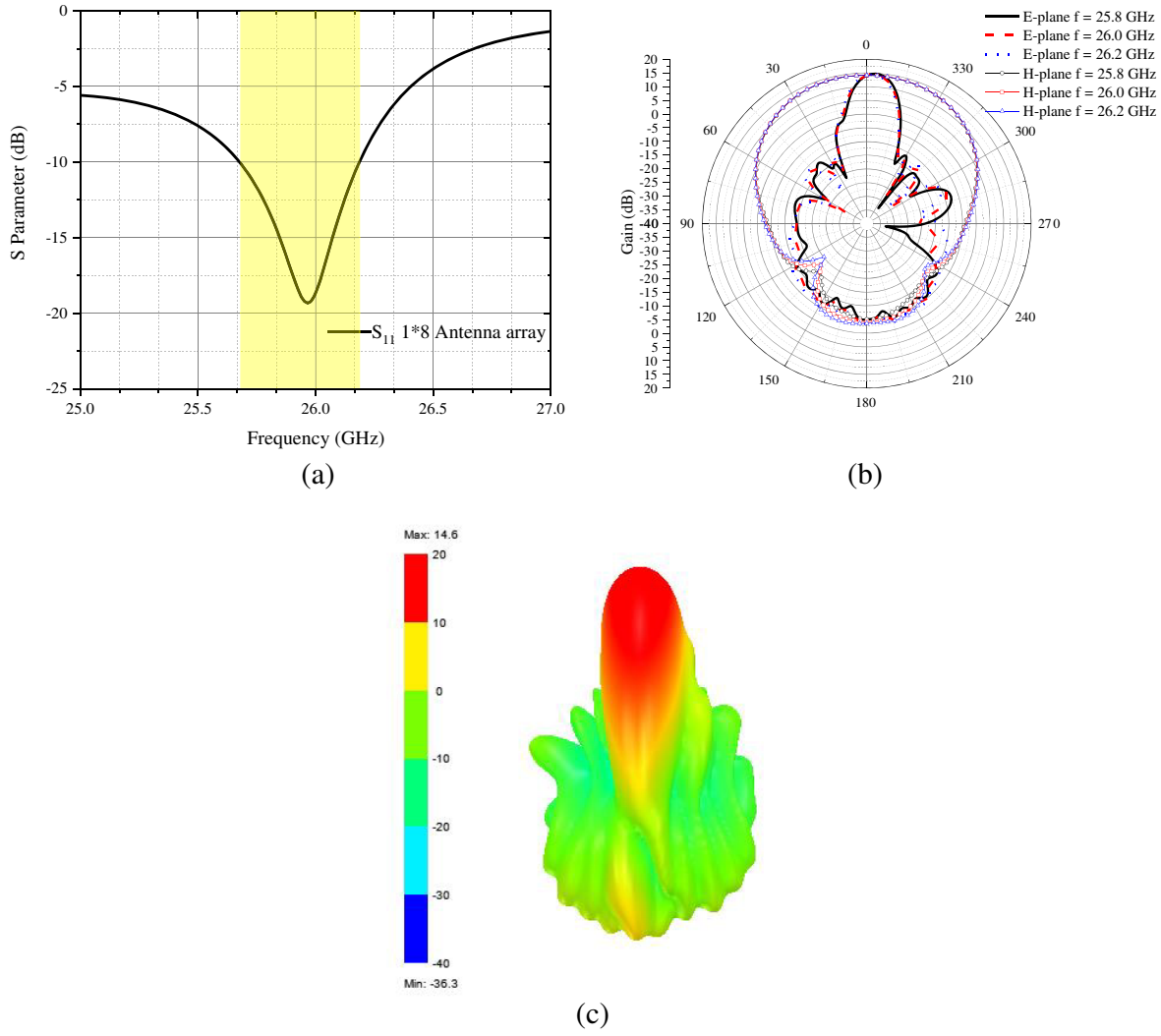

Figure 9. Simulated antenna performance of 8-element line array. (a) S parameters. (b) 2-D radiation patterns vary with frequency. (c) 3-D radiation pattern at 26 GHz.

Then, the characteristics of the two kinds of feed network are compared and analyzed.

The series-parallel hybrid feed network has a symmetrical structure, whose equivalent circuit model is shown in Fig. 10. Y_{in1} and Y_{in} are the input admittance of planar array and the input admittance of one side of planar array, respectively. Y_{c1} is the characteristic admittance of main feeder line. Y_{c2} is the characteristic admittance of quarter impedance matcher at the end of linear array, and λ_g is the wavelength in waveguide. The ratio relation of admittances is given based on the equivalent circuit

$$Y_i' = \left(\frac{Y_{c1}}{Y_{c2}}\right)^2 Y_{i+1} = n_i^2 Y_{i+1} \tag{4}$$

where n_i is the ratio of characteristic admittance of main feeder line to the one of each branch feeder line. Then the input admittance Y_i for each array element is defined as

$$Y_i = Y_A + n_i^2 Y_{i+1} \tag{5}$$

where Y_A is the characteristic admittance of each DRA element. Furthermore, the input impedance of each side of parallel circuit is given as

$$Z_{in} = \frac{Z_A}{1 + n_1^2 + n_1^2 n_2^2 + \ldots + n_1^2 n_2^2 \ldots n_{n-1}^2} \tag{6}$$

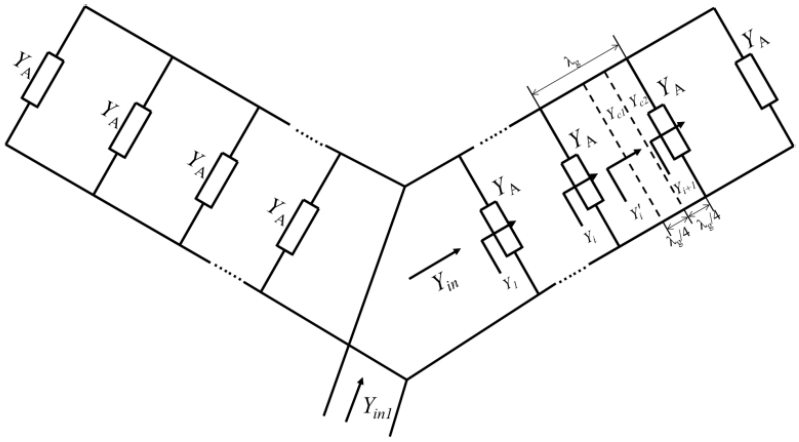

Figure 10. Equivalent circuit of series-parallel hybrid feed network.

According to the input impedance of each transmission line, the length and width of the microstrip feeders can be calculated by the microstrip line calculation tool [24].

The eight linear arrays are connected by traveling wave series feed on both sides of the hybrid series-parallel feed network, and the T-type power divider is used to feed the two sides of the antenna in parallel, as shown in Fig. 11. In order to keep the same phase of each array element, the interval of the output ports is one dielectric wavelength, which is realized by the meander microstrip lines. Table 3 shows the structure parameters of the series-parallel hybrid feed network. The proportional relationship of current excitation for each output port is $I_1 : I_2 : I_3 : I_4 = 1 : 0.83 : 0.57 : 0.35$, which obeys the Chebyshev distribution. The hybrid feed network is connected to the array elements with $\lambda_g/4$ impedance conversion section.

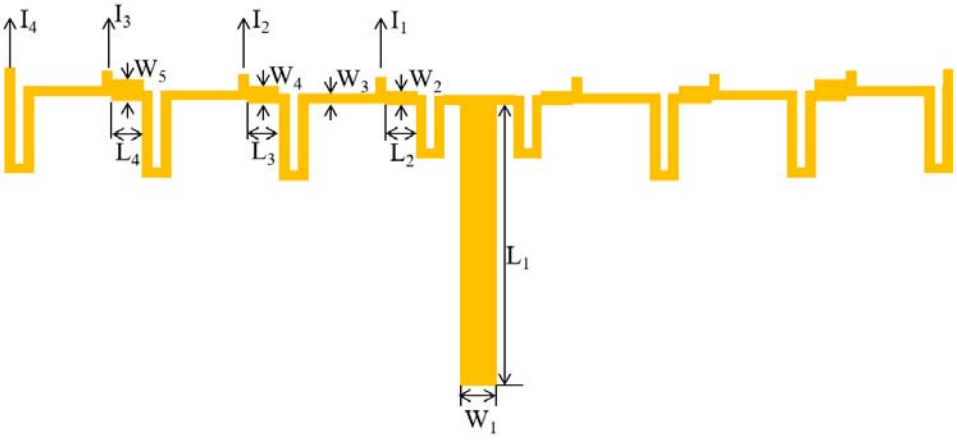

Figure 11. Configuration of series-parallel hybrid feed network.

Table 3. Structural parameters of series-parallel hybrid feed network.

Parameter	W_1	W_2	W_3	W_4	W_5
Value (mm)	0.99	0.69	0.19	0.52	1.00
Parameter	L_1	L_2	L_3	L_4	
Value (mm)	13.34	1.59	1.14	1.60	

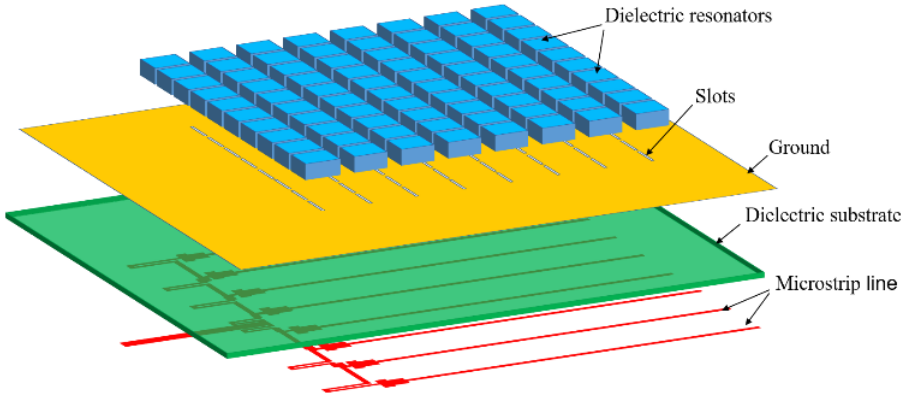

Figure 12. 8×8 planar array fed by series-parallel hybrid feed network.

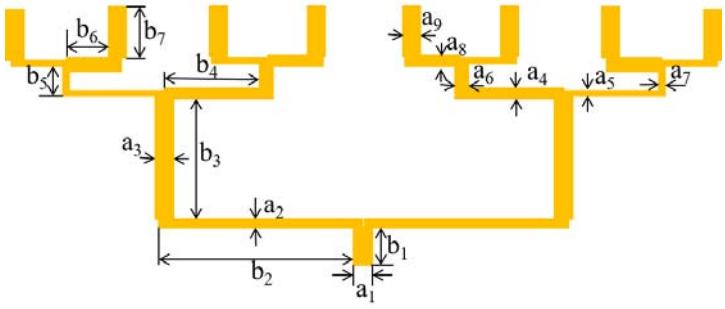

Figure 13. Configuration of parallel-cascaded feed network.

Table 4. Structural parameters of parallel-cascaded feed network.

Parameter	a_1	a_2	a_3	a_4	a_5	a_6	a_7	a_8	a_9
Value (mm)	0.78	0.37	0.78	0.63	0.20	0.63	0.20	0.70	0.89
Parameter	b_1	b_2	b_3	b_4	b_5	b_6	b_7		
Value (mm)	2.12	10.99	6.70	5.29	1.32	2.35	2.87		

Figure 12 shows the 8×8 planar array fed by the series-parallel hybrid feed network, which consists of four layers. The top layer is the radiation array which is composed of DRAs and located on the slotted metal ground of the PCB. The dielectric substrate is Arlon DiClad 880 in the middle layer, and the bottom layer is the hybrid feed network.

For the sake of discussing the performance of feed network, the parallel-cascaded feed network is also designed, which is composed of 3 levels of power dividers, as shown in Fig. 13. The structure parameters of the parallel-cascaded feed network are shown in Table 4. The feed network consists of 1 equal power divider and 3 unequal power dividers. The current excitation of each linear array follows the Chebyshev distribution with the adjustment of unequal power divider ratio. The planar array fed by parallel-cascaded power dividers is shown in Fig. 14, in which the linear arrays are also fed by the traveling wave series method shown in Fig. 5.

The series-parallel hybrid feed network and parallel-cascaded feed network are compared based on the impedance matching and radiation performance. Fig. 15 shows S_{11} parameters of the input ports for two different feeding methods. It is found that the series-parallel hybrid feed network has obvious advantages in the impedance bandwidth. The radiation patterns are compared at 26 GHz operation

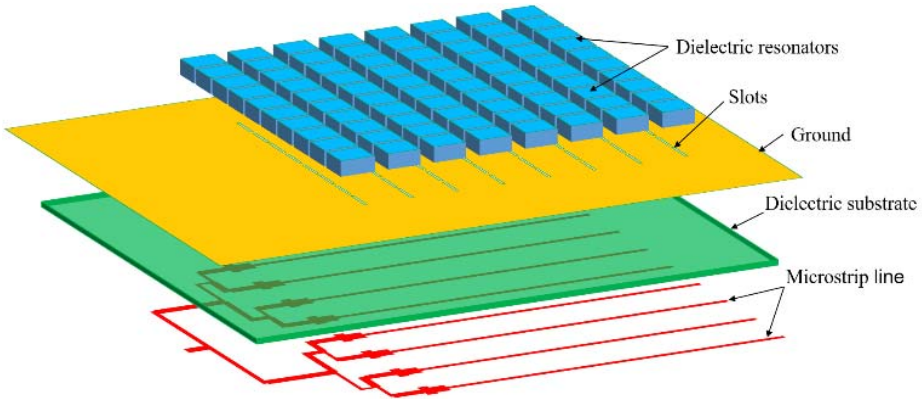

Figure 14. 8×8 planar array fed by parallel-cascaded feed network.

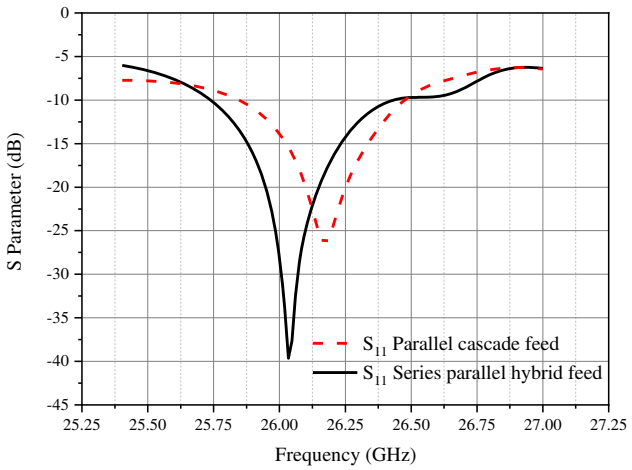

Figure 15. S parameters of planar array excited with different feed networks.

Table 5. Performance comparison of DRA array and patch antenna array.

	DRA array	Patch Antenna array
Bandwidth (MHz)	830	600
Gain (dBi)	21.3 ~ 21.5	20.4 ~ 21.3
Side Lobe Level (dB) E Plane	25.3	19.0
Side Lobe Level (dB) H Plane	29.4	18.8
Radiation Efficiency (26 GHz)	92.45%	82.42%
Front Back Ratio (dB)	14.8	23.1

frequency in Fig. 16. It is obvious that the antenna array fed by the series-parallel hybrid feed network can effectively suppress the sidelobe, and its antenna gain is slightly higher than that of the parallel-cascaded feed method. Although the parallel-cascaded feed network has the advantages of symmetrical and simple structure, the bandwidth of the unequal power divider will directly affect the performance of the feed network. Moreover, the parallel-cascaded feed network needs more PCB area, which is not conducive to antenna miniaturization design.

Therefore, this paper selects the series-parallel hybrid feed network to feed the planar array and

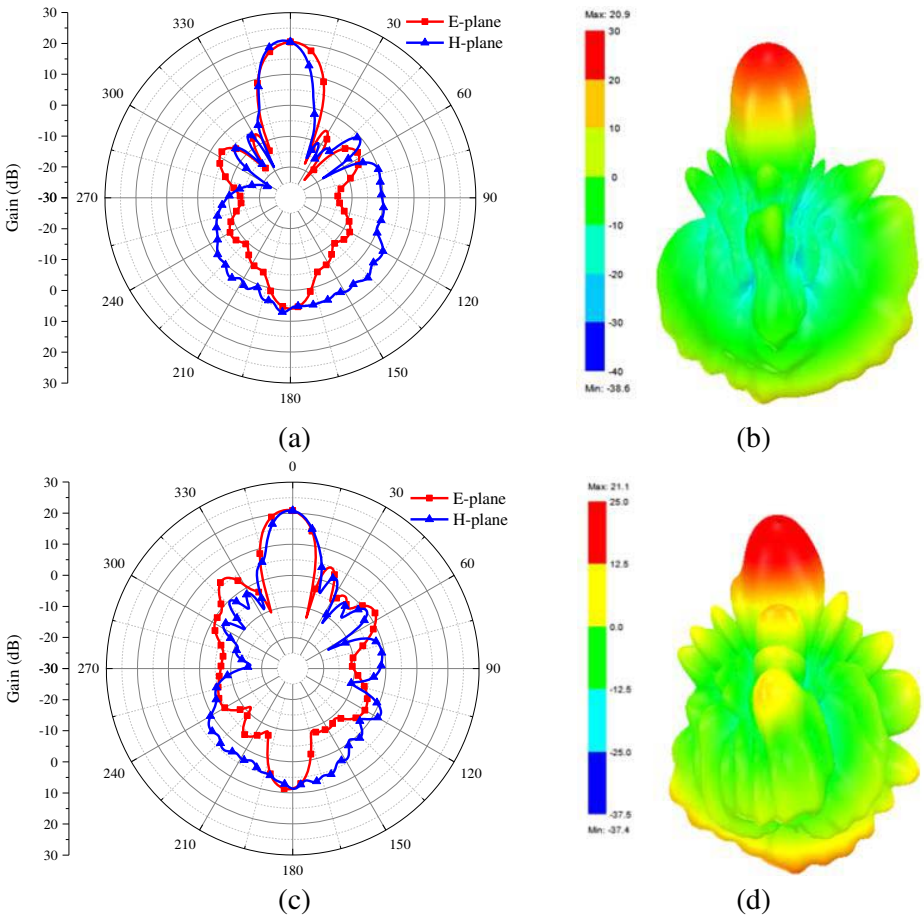

Figure 16. Radiation patterns of planar array excited with different feed networks. (a) 2-D patterns of series-parallel hybrid feed network. (b) 3-D pattern of series-parallel hybrid feed network. (c) 2-D patterns of parallel-cascaded feed network. (d) 3-D pattern of parallel-cascaded feed network.

comprehensively considers the mutual coupling relationship between the antenna array and the feed network to optimize the design of the planar array. As shown in Fig. 17, the planar array antenna has good pattern convergence in the frequency range 25.75 GHz–26.35 GHz.

In order to evaluate the performance of the proposed DRA array, the planar patch antenna array is simulated and compared with the DRA array fed by series-parallel hybrid network. There are also 8×8 elements in the patch antenna array, which are fed by the microstrip line, as shown in Fig. 18(a). Due to the two-dimensional structure of patch antenna array, the impedance bandwidth of the DRA array is apparently wider than that of patch array in Fig. 18(b). It is also found that the gain of DRA array is higher and is more stable in the operation frequency band in Fig. 18(c). Fig. 18(d) shows that the SLL of DRA array is obviously suppressed, and the beamwidths in E-plane and H-plane are similar. Moreover, the first null of DRA array pattern is much deeper, which is suitable for directional transmission information. Nevertheless, the lower front back ratio of DRA array is also obvious, which is caused by the backward leakage of radiation from the feeding apertures. The parameters comparison of the DRA array and patch antenna array is shown in Table 5 in detail. The DRA obtains higher radiation efficiency, since there is no conductor loss in the radiator.

4. MEASUREMENTS

According to the optimal size optimized by simulation, a planar array fed by a series parallel hybrid feed network is fabricated, as shown in Fig. 19. The DRAs are located on the upper surface of the antenna

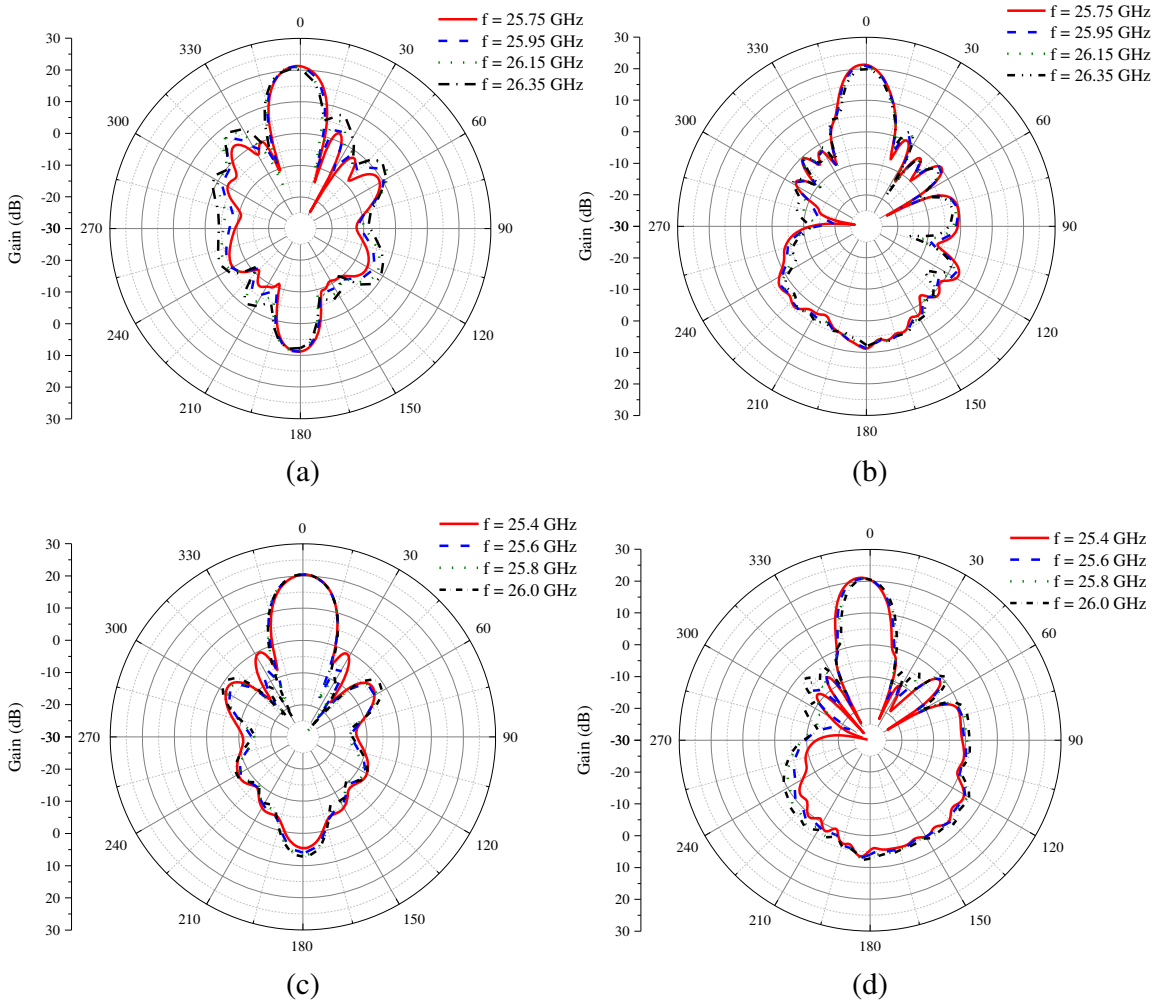

Figure 17. Radiation patterns of different operation frequencies. (a) E-plane patterns of series-parallel hybrid feed network. (b) H-plane patterns of series-parallel hybrid feed network. (c) E-plane patterns of parallel-cascaded feed network. (d) H-plane patterns of parallel-cascaded feed network.

structure, and the lower surface is the series-parallel hybrid feed network. The length and width of the antenna prototype are 87.1 mm and 73.70 mm, respectively. The small-size planar structure antenna is desirable to integrate on the vehicle platform for DFRC system.

The S parameters and radiation performance are measured in a microwave anechoic chamber. Fig. 20(a) shows the reasonable consistency between the measurement and simulation results of S parameter. The measured impedance bandwidth of less than -10 dB is 570 MHz (25.77 GHz–26.34 GHz), which verifies the good impedance matching characteristics. Fig. 20(b) shows the comparison of gain patterns of measurements and simulations, in which the simulated HPBWs and tested ones are $17 \pm 1^\circ$ and $17 \pm 2^\circ$, respectively. The antenna gain is 20.5 ± 1 dBi. It is apparent that the SLL of antenna array is greater than 20 dB, which meets the design requirements. However, the back lobe of the antenna is also obvious, which is caused by the slot coupling feed mode and the prototype processing precision. Since the antenna arrays are commonly mounted on the metal structure of vehicle equipment, the backward radiation could be suppressed. Furthermore, the electric reflector, such as SIW cavity and metalized surface, could be used to increase the Front-Back Ratio (FBR) of antenna array.

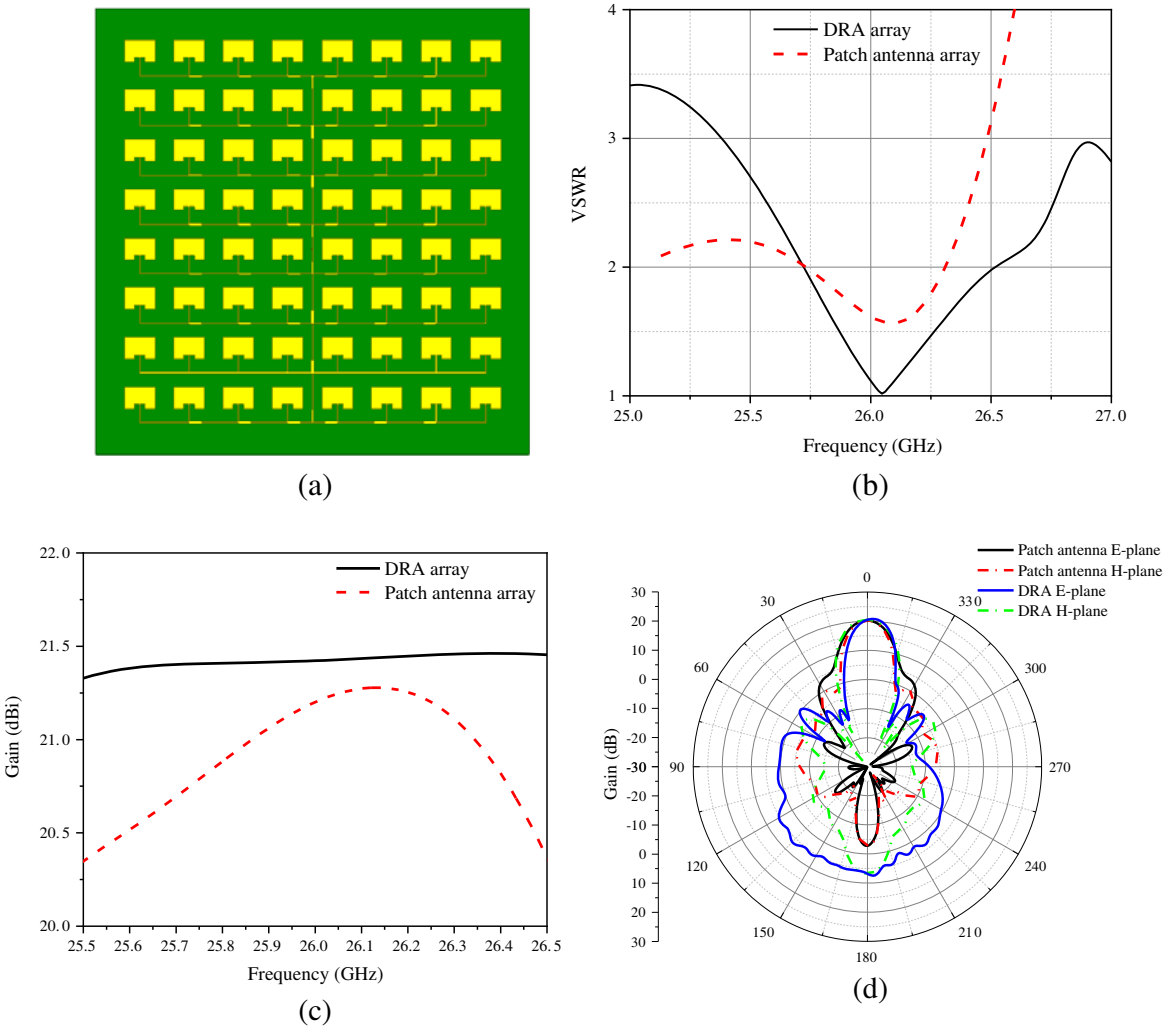

Figure 18. Comparison of DRA array and patch antenna array. (a) Top view of planar patch antenna array. (b) Voltage Standing Wave Ratio (VSWR). (c) Gain. (d) Radiation Pattern.

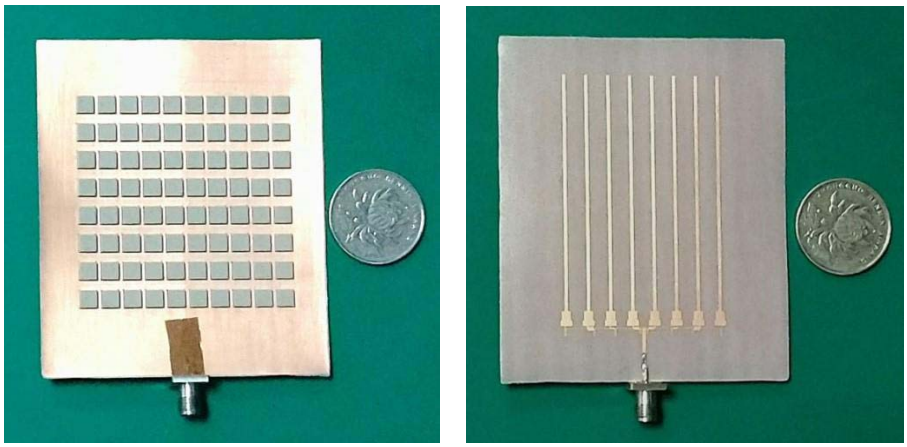

Figure 19. Prototype of planar antenna array fed by series-parallel hybrid feed. (a) Top view. (b) Bottom view.

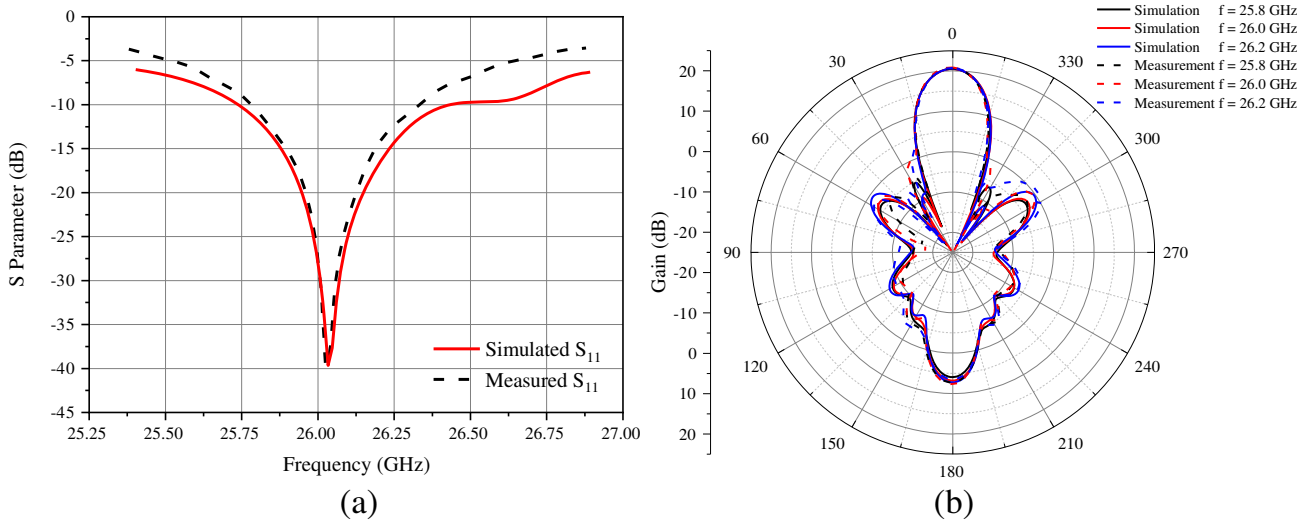

Figure 20. Measured and simulated results of planar antenna array fed by series-parallel hybrid feed. (a) S parameters S_{11}. (b) Radiation patterns.

5. CONCLUSION

In this paper, a novel planar DRA array is proposed for the vehicle wireless communication in millimeter wave band, which consists of eight 8-element linear arrays. Each element of the linear array is fed with a coupling aperture of the standing-wave series feed network. According to the aperture coupling model of DRA, the excitation magnitude of each DRA element is optimized by the position and size of the feeding slot. Considering the performance of impedance band width, the linear arrays are unequally fed with the series-parallel hybrid feed network to achieve the 8×8 planar array. The wireless communication capacity could be significantly promoted with the millimeter wave technology, and the automotive product design requires miniaturized communication equipment. Due to the absence of conducting material, the DRA array is characterized by high radiation efficiency especially for millimeter wave band when the low-loss dielectric material is chosen. Since the proposed DRA array with excellent electrical performance and stable structure could be installed on the front/back bumper or windshield of the automobiles, it is a promising candidate for the transceivers in the 5G and IoV network.

ACKNOWLEDGMENT

The authors would like to thank the anonymous reviewers for their invaluable comments and suggestions, which lead to great improvement of our manuscript. This work is supported by the Science and Technology Research Program of Chongqing Municipal Education Commission [grant No. KJQN202000623], National Natural Science Foundation of China [grant No. 61871063, 41606203], and the Chongqing basic Science and Frontier Technology Research Project (cstc2017jcyjAX0193).

REFERENCES

1. Guan, K., et al., "5-GHz obstructed vehicle-to-vehicle channel characterization for internet of intelligent vehicles," *IEEE Internet of Things Journal*, Vol. 6, No. 1, 100–110, Feb. 2019.
2. Zhong, Z., et al., "A compact dual-band circularly polarized antenna with wide axial-ratio beamwidth for vehicle GPS satellite navigation application," *IEEE Transactions on Vehicular Technology*, Vol. 68, No. 9, 8683–8692, Sept. 2019.

3. Wang, Z., H. Liu, S.-J. Fang, and Y. Cao, "A low-cost dual-wideband active GNSS antenna with low-angle multipath mitigation for vehicle applications," *Progress In Electromagnetics Research*, Vol. 144, 281–289, 2014.
4. Schwarz, S., E. Zöchmann, M. Müller, and K. Guan, "Dependability of directional millimeter wave vehicle-to-infrastructure communications," *IEEE Access*, Vol. 8, 53162–53171, 2020.
5. Ko, M., H. Lee, and J. Choi, "Planar LTE/sub-6 GHz 5G MIMO antenna integrated with mmWave 5G beamforming phased array antennas for V2X applications," *IET Microwaves, Antennas & Propagation*, Vol. 14, No. 11, 1283–1295, 2020.
6. Sharma, A., et al., "Communication and networking technologies for UAVs: A survey," *Journal of Network and Computer Applications*, Vol. 168, 1–24, 2020.
7. Hassanien, A., M. G. Amin, E. Aboutanios, and B. Himed, "Dual-function radar communication systems: A solution to the spectrum congestion problem," *IEEE Signal Processing Magazine*, Vol. 36, No. 5, 115–126, Sept. 2019.
8. Xu, J., et al., "Wideband, low-profile patch array antenna with corporate stacked microstrip and substrate integrated waveguide feeding structure," *IEEE Transactions on Antennas and Propagation*, Vol. 67, No. 2, 1368–1373, Feb. 2019.
9. Inomata, M., et al., "Transparent glass antenna for 28 GHz and its signal reception characteristics in urban environment," *2020 14th European Conference on Antennas and Propagation (EuCAP)*, 1–5, Copenhagen, 2020.
10. Trujillo-Flores, J. I., et al., "CPW-fed transparent antenna for vehicle communications," *Applied Sciences*, Vol. 10, 1–11, 2020.
11. Desai, A., T. Upadhyaya, M. Palandoken, and C. Gocen, "Dual band transparent antenna for wireless MIMO system applications," *Microwave and Optical Technology Letters*, 1–12, 2019.
12. Boyuan, M., J. Pan, E. Wang, and Y. Luo, "Fixing and aligning methods for dielectric resonator antennas in K band and beyond," *IEEE Access*, Vol. 7, 12638–12646, 2019.
13. Chowdhury, R. and R. K. Chaudhary, "Investigation of new sectored hemispherical dielectric resonator antennas operating at TM_{101} and TE_{111} mode for circular polarization," *Progress In Electromagnetics Research*, Vol. 167, 95–109, 2020.
14. Sharma, A., G. Das, S. Gupta, and R. K. Gangwar, "Quad-band quad-sense circularly polarized dielectric resonator antenna for GPS/CNSS/WLAN/WiMAX applications," *IEEE Antennas and Wireless Propagation Letters*, Vol. 19, No. 3, 403–407, Mar. 2020.
15. Yang, M., Y. Pan, Y. Sun, and K. Leung, "Wideband circularly polarized substrate-integrated embedded dielectric resonator antenna for millimeter-wave applications," *IEEE Transactions on Antennas and Propagation*, Vol. 68, No. 2, 1145–1150, Feb. 2020.
16. Mazhar, W., D. M. Klymyshyn, G. Wells, A. A. Qureshi, M. Jacobs, and S. Achenbach, "Low-profile artificial grid dielectric resonator antenna arrays for mm-wave applications," *IEEE Transactions on Antennas and Propagation*, Vol. 67, No. 7, 4406–4417, Jul. 2019.
17. Keyrouz, S. and D. Caratelli, "Dielectric resonator antennas: Basic concepts, design guidelines, and recent developments at millimeter-wave frequencies," *International Journal of Antennas and Propagation*, Vol. 2016, 4406–4417, 2016.
18. Pan, Y. M., X. Qin, Y. X. Sun, and S. Y. Zheng, "A simple decoupling method for 5g millimeter-wave MIMO dielectric resonator antennas," *IEEE Transactions on Antennas and Propagation*, Vol. 67, No. 4, 2224–2234, Apr. 2019.
19. Zhong, L., D. Zhou, R. Liu, X. Wang, and X. Meng, "The feasibility of coexistence between IMT-2020 and inter-satellite service in 26 GHz band," *2020 International Wireless Communications and Mobile Computing (IWCMC)*, 1006–1011, Limassol, 2020.
20. Jin, L., R. Lee, and I. Robertson, "A dielectric resonator antenna array using dielectric insular image guide," *IEEE Transactions on Antennas and Propagation*, Vol. 63, No. 2, 859–862, Feb. 2015.
21. Diawuo, H. A. and Y. Jung, "Broadband proximity-coupled microstrip planar antenna array for 5G cellular applications," *IEEE Antennas and Wireless Propagation Letters*, Vol. 17, No. 7, 1286–1290, Jul. 2018.

22. Ma, T., J. Ai, M. Shen, and W. T. Joines, "Design of novel broadband endfire dipole array antennas," *IEEE Antennas and Wireless Propagation Letters*, Vol. 16, 2935–2938, 2017.
23. Qasaymeh, Y. M., A. Almuhasien, and T. Kamran, "A compact wideband series linear dielectric resonator array antenna," *Turkish Journal of Electrical Engineering & Computer Sciences*, Vol. 28, 394–403, 2020.
24. Yi, H., L. Li, J. Han, and Y. Shi, "Traveling-wave series-fed patch array antenna using novel reflection-canceling elements for flexible beam," *IEEE Access*, Vol. 7, 111466–111476, 2019.